Accepted Manuscript

Determination of gaseous fission product behavior near the cerium dioxide Σ3 (111) [11¯0] tilt grain boundary via first-principles study

Jianqi Xi, Bin Liu, Haixuan Xu, Yanwen Zhang, William J. Weber

PII: S0022-3115(17)31039-5

DOI: 10.1016/j.jnucmat.2017.11.046

Reference: NUMA 50655

To appear in: *Journal of Nuclear Materials*

Received Date: 21 July 2017

Revised Date: 18 October 2017

Accepted Date: 27 November 2017

Please cite this article as: J. Xi, B. Liu, H. Xu, Y. Zhang, W.J. Weber, Determination of gaseous fission product behavior near the cerium dioxide Σ3 (111)[11¯0] tilt grain boundary via first-principles study, *Journal of Nuclear Materials* (2017), doi: 10.1016/j.jnucmat.2017.11.046.

Determination of gaseous fission product behavior near the cerium dioxide Σ3 (111)/[1$\bar{1}$0] tilt grain boundary via first-principles study

Jianqi Xi,[1] Bin Liu,[2] Haixuan Xu,[1] Yanwen Zhang,[3,1] William J. Weber[1,3,*]

[1] *Department of Materials Science and Engineering, University of Tennessee, Knoxville, Tennessee 37996, USA*

[2] *School of Materials Science and Engineering, Shanghai University, Shanghai, 200444, China*

[3] *Materials Science and Technology Division, Oak Ridge National Laboratory, Oak Ridge, Tennessee 37831, USA*

Abstract

Grain boundaries (GBs) are the most abundant structural defects in nanostructured nuclear fuels and play an important role in determining fission product behavior, which further affects the performance of nuclear fuels. In this work, cerium dioxide (CeO_2) is used as a surrogate material for mixed oxide fuels to understand gaseous fission product behavior, specifically Xe. First-principles calculations are employed to comprehensively study the behavior of Xe and trap sites for Xe near the Σ3 (111)/[1$\bar{1}$0] grain boundary in CeO_2, which will provide guidance on overall trends for Xe stability and diffusion at grain boundaries vs in the bulk. Significant segregation behavior of trap sites, regardless of charge states, is observed near the GB. This is mainly ascribed to the local atomic

[*] *Department of Materials Science and Engineering, University of Tennessee, Knoxville, Tennessee 37996, USA, E-mail: wjweber@utk.edu; Tel:+1-865-974-0415*

structure near the GB, which results in weaker bond strength and more negative segregation energies. For Xe, however, the segregation profile near the GB is different. Our calculations show that, as the size of trap sites increases, the segregation propensity of Xe is reduced. In addition, under hyper-stoichiometric conditions, the solubility of Xe trapped at the GB is significantly higher than that in the bulk, suggesting higher Xe concentration than that in the bulk. The results of this work demonstrate that the diffusion mechanism of Xe in CeO_2 is comparable to that in UO_2. The diffusion activation energies of Xe atoms in the Σ3 GB are lower than that in the bulk CeO_2. These results suggest that the diffusivity of Xe atoms is higher along the GB than that in the bulk, which enhances the aggregation of Xe atoms near the GB.

Keywords

Grain Boundary; Fission Product; Segregation and Diffusion; First Principles Calculations; Cerium Dioxide

1. Introduction

Nanocrystalline (NC) fluorite-oxides (Urania (UO_2), Zirconia (ZrO_2), Ceria (CeO_2), etc.) with grain sizes below 100 nm are known to exhibit improved chemical and physical properties, as well as enhanced radiation resistance compared with their microcrystalline and bulk counterparts [1-8]. Due to their excellent properties, NC fluorite-oxides have been proposed for potential use as nuclear fuels and inert matrix fuels in advanced nuclear energy systems [1-3]. Many experimental studies on NC oxides have reported that nanostructured fuels possess the ability to more efficiently relax the interaction stresses between the cladding and fuel due to much higher plasticity [3-6], and they are more resilient to radiation damage than corresponding large-grained materials owing to the complex nanostructure and enhanced defect recombination at their multiple grain boundaries (GBs) [3, 6-8]. On the other hand, post-irradiation annealing leads to gas bubble growth near the GBs in the NC oxides that indicates higher thermally induced swelling compared to the larger-grained material due to accelerated fission gas diffusion and higher vacancy concentration in the NC oxides at high temperatures [3]. The uncertain role of GBs in irradiation resistance performance indicates that many fundamental questions on the interaction between irradiation-induced defects and GBs still remain unsolved. An outstanding question is the nature of defect behavior at GBs, which affects both microstructural evolution and material properties by altering the local atomic structure and energy landscape for mass transport [10].

To elucidate the underlying cause of defect behavior in oxide fuels, several modeling and simulation studies based on both empirical potentials [11-18] and density functional theory (DFT) have been performed [19-25]. Catlow and Grimes [11-14] have conducted

a series of molecular dynamics simulations to investigate the stability of trap sites in the bulk and grain interior, and concluded that the mono-vacancy (V_M), di-vacancy (V_M-V_O), and Schottky defect (V_M-$2V_O$) can be regarded as stable trap sites for fission products in MO_2 (M=U, Th, Ce, Zr, Pu). These results are further confirmed by DFT calculations [19-25]. Meanwhile, the bulk-diffusion mechanism of fission products in MO_2 has also been determined, and the results indicate that the vacancy-assisted diffusion mechanism is dominant for the fission products [19, 20]. Andersson et al. [21] have further suggested that the diffusion of trapped fission products in UO_2 could be realized by binding a second trap site. Recently, Nerikar et al. [26] have studied how the GBs affect the segregation behavior of Xe in UO_2, and they found that the segregation of Xe is more energetically favorable in highly disordered GBs than in the GBs with a low energy. While providing qualitative insights, properties of these various defects near GBs, such as the stability and diffusion behavior, are still not well understood.

In this work, CeO_2 is studied as a model compound. It is often employed as a nonradioactive surrogate in experimental studies of nuclear fuel systems, since it has the same fluorite-type structure and many similar material properties, such as melting point and thermal conductivity, as UO_2 and plutonium dioxide (PuO_2) [27, 28]. In addition, microstructural evolution under particle bombardment at low doses in CeO_2 is also similar to that in low-burnup UO_2 fuels [29, 30]. In order to better understand the influence of the interaction between GBs and defects on the irradiation response of NC oxides, the behavior of native cation vacancies and vacancy clusters near GBs, as potential trap sites for fission products, are systematically investigated using first-principles calculations. Moreover, the segregation and solution profile of Xe, a major

fission gas, on these sites are considered. Finally, the diffusion of Xe in the GB region of CeO_2 is discussed and compared with that in the bulk region, which lead to better understanding of high-density of gas bubbles near the GBs [9]. Our analysis is focused on the experimentally identified $\Sigma3(111)/[1\bar{1}0]$ tilt GB. Since the GB energy of Σ3 is lower than other GBs in CeO_2, and there are evidences that GBs with a low energy provide a lower propensity toward impurity segregation [26, 31] and diffusion [32, 33], we expect that our investigation of the $\Sigma3(111)/[1\bar{1}0]$ tilt GB will provide a lower bound estimate for defect segregation and diffusion in NC CeO_2.

2. Methodology and Simulation Details

DFT calculations are performed with the Vienna Ab-Initio Simulation Package (VASP) code in terms of the projector augmented wave method (PAW) [34]. The PAW potentials for Ce, O, and Xe contains 12, 6, and 8 valence electrons (Ce: $5s^2 5p^6 4f^1 5d^1 6s^2$, O: $2s^2 2p^4$, and Xe: $5s^2 5p^6$), respectively. The local density approximation (LDA) [35], coupled with Hubbard on-site Columbic correction [36] and spin-polarized calculation, is employed. The effective U_{eff}, (U-J), is taken as 6 eV [37] to correctly capture the localization of 4*f* electrons for Ce. The calculated lattice constant of 5.418 Å is consistent with the experimental value of 5.412 Å [38]. The $\Sigma3(111)/[1\bar{1}0]$ tilt GB is generated by mirroring and shifting the (111) plane based on knowledge from both theoretical and experimental results [39, 40], as shown in Fig. 1. It should be noted that the cation and anion sublattices are nearly mirror symmetrical to the cation and anion mirror planes, respectively; and the Ce sites within the Ce_{-1} layer has local atomic environments of seven-fold coordination with oxygen ions, while they are of eight-fold coordination in the bulk area of CeO_2. After carefully checking for convergence with respect to the GB

energy, we confirm that the supercell with dimensions 31.21 Å × 7.56 Å × 13.10 Å, with 240 atoms, is sufficient for convergence the force and energy criteria described below. Different cation layers are considered near the GB, as labeled in Fig. 1. All computations are performed with a Monkhorst-Pack 2×2×1 k-mesh and a plane-wave cutoff energy of 400 eV. Errors from both the cutoff and the k-point convergence are less than 1 meV/atom. Structures and atomic coordinates are fully relaxed until forces on the ions converged to below 0.02 eV/Å. The migration barriers in this work are calculated in the DFT+*U* framework using the climbing image nudged elastic band method (CI-NEB) [41-43].

The formation energies, E_f, of different defects, which may act as possible trap sites for Xe, have been evaluated, as described previously [10, 42] using the following expression:

$$E_f(\text{defect}, q) = E_{\text{T}}(\text{defect}, q) - E_{\text{T}}(\text{perfect}) + \sum_i n_i \mu_i + q\left(\varepsilon_{\text{F}} + E_{\text{VBM}}^{\text{perfect}} + \left(V_{av}^{\text{defect}} - V_{av}^{\text{perfect}}\right)\right) \quad (1)$$

where $E_{\text{T}}(\text{defect}, q)$ is the total energy of a CeO_2 supercell with one defect in charge state q, and $E_{\text{T}}(\text{perfect})$ is the total energy of the host supercell. n_i is the number of atoms of type i removed from ($n_i > 0$) the system to form vacancies, μ_i is the chemical potential of atom i. The chemical potentials for oxygen and cerium, as reported in Table I, are determined by the following thermodynamic limits: (1) the limit of CeO_2 stoichiometry, $\mu_{\text{Ce}}(\text{CeO}_2) + \mu_{\text{O}}(\text{CeO}_2) = \mu_{\text{CeO}_2}(\text{bulk})$; (2) the upper limit of the system against decomposition into its constituent elements, $\mu_{\text{Ce}} \leq \mu_{\text{Ce}}(\text{bulk})$, and $\mu_{\text{O}} \leq \mu_{\text{O}}(\text{bulk})$; and the lower limit is that $\mu_{\text{Ce}}(\text{CeO}_2) \geq \mu_{\text{CeO}_2}(\text{bulk}) - \mu_{\text{Ce}}(\text{bulk})$, and $\mu_{\text{O}}(\text{CeO}_2) \geq \mu_{\text{CeO}_2}(\text{bulk}) - \mu_{\text{O}}(\text{bulk})$. In this work, molecular O_2 gas is simulated by

putting an oxygen dimer in a vacuum box, as discussed in detail elsewhere [42]. ε_F is the Fermi level measured from the valence band maximum (VBM), which changes within the band gap, E_g ~2.64 eV, from the VBM to the lowest unoccupied Ce *4f* state. $E_{\mathrm{VBM}}^{\mathrm{perfect}}$ is the VBM in the perfect system. The term $\left(V_{av}^{\mathrm{defect}} - V_{av}^{\mathrm{perfect}}\right)$ in Eq. (1) is the electronic potential alignment correction for the E_{VBM}, which is discussed elsewhere [10, 42]. This alignment is necessary for finite size supercells with defects under periodic boundary conditions, since E_{VBM} in a defective supercell is generally different from that in a perfect supercell. The formation energies, E_f^{GB}, of cation vacancies and vacancy clusters at the GB and in the vicinity of the GB are determined as a function of the cation positions and summarized in the Supplementary material, as shown in Fig. S1. The segregation energy, E_{seg}, for these defects is thus calculated as:

$$E_{\mathrm{seg}} = E_f^{\mathrm{GB}}(\mathrm{defect}) - E_f^{\mathrm{bulk}}(\mathrm{defect}) \qquad (2)$$

where the reference energy is the formation energy of the defect in the pure bulk with the same number of atoms as that in the GB system. Since our current work mainly focuses on the determination of the segregation profiles for these defects near the GB, and our results in different size supercells have a similar segregation profile, as shown in Fig. S5, we can confirm that the selection of reference energy in the calculation of segregation energy has no effect on our conclusions. The configuration of a Schottky defect in the bulk is selected as V_{Ce} with two V_Os along the (110) direction, which has the lowest formation energy, as shown in Table SI (Supplementary materials).

In order to investigate the stability of Xe trapped near the GB, we determine the solution energies in these possible trap sites. For reference, the energies in the bulk are also calculated. The solution energy $E_{\mathrm{Xe}}^{\mathrm{sol}}$ is defined as the energy required to accommodate

one Xe atom assumed to be at infinity to a trap site under thermodynamic equilibrium [13]:

$$E_{\mathrm{Xe}}^{\mathrm{sol}} = E_{\mathrm{T}}(\mathrm{Xe, trap\ site}, q) - E_{\mathrm{T}}(\mathrm{perfect}) - E_{\mathrm{Xe}} + \sum_i n_i \mu_i + q\left(\varepsilon_{\mathrm{F}} + E_{\mathrm{VBM}}^{\mathrm{perfect}} + \Delta V\right) \quad (3)$$

Where $E_{\mathrm{T}}(\mathrm{Xe, trap\ site})$ is the total energy of the system with Xe at the trap site, E_{Xe} is the total energy of an isolated Xe atom, and ΔV is the potential alignment for the system with the fission product, as defined in Eq. (1).

3. Results and Discussion

3.1 Segregation of cation vacancy

The calculated segregation energies for V_{Ce} with different charge states at the GB and its vicinity are shown in Fig. 2. For V_{Ce}, regardless of the charge states, a significant segregation to the Ce_{-1} layer is observed, with segregation energies of -0.84 eV to -1.66 eV. Similarly, the segregation energies to Ce_0 layer are also favorable, -0.79 to -1.29 eV, suggesting the possible accumulation of V_{Ce} in these layers that are possible nucleation sites for gaseous fission products. The segregation energies for V_{Ce} in other layers are close to zero, which is similar to the bulk behavior. To understand these results, we propose the following model: the formation of one V_{Ce} is attributed to two contributions [44, 45]: breaking the chemical bonds of a Ce atom that yields the bond energy, E_{bond}; and the local geometrical relaxations that releases the relaxation energy, E_{relax}. Accordingly, E_{seg} can be written as the sum of the two terms, $E_{\mathrm{seg}} = E_{\mathrm{bond}} + E_{\mathrm{relax}}$, in which the values of E_{bond} and E_{relax} are referenced to their bulk values. Fig. 2 (b) shows the layer dependent values of E_{bond} and E_{relax} for V_{Ce}^{0}. The following striking features can be

perceived from Fig. 2 (b): (i) both E_{bond} and E_{relax} change similarly to E_{seg}, with a minimum in the Ce_{-1} layer; (ii) E_{bond} has a larger value compared with E_{relax}. These features clearly suggest that E_{bond} is a more dominating term than E_{relax} in determining the overall trends of the V_{Ce}^{0} segregation profile. To better understand these features, we characterize the bond strengths and analyze local structural relaxation in different layers. It is found that the local atomic structure near the GB is mainly responsible for the weaker bond strength and more negative segregation energies. Detailed information is provided in the Supplementary material, as shown in Fig. S3 and Fig. S4.

3.2 Segregation profile of cation vacancy cluster

Cation vacancy clusters, consisting of one cation vacancy and its nearest-neighboring V_Os [21], have several different configurations depending on the V_O position near the GB; thus, it is difficult to identify the most stable configuration. In order to determine a general trend, we consider all the possible configurations of these defects in different charge states. Fig. 3 (a) describes the defects in the formal charge states i.e., V_{Ce}^{4-}, $(V_{Ce}\text{-}V_O)^{2-}$, $(V_{Ce}\text{-}2V_O)^{0}$. The lowest segregation energy for vacancy clusters at different charge states, which corresponds to the most stable configuration, are provided in Fig. 3 (b) and (c). It is found that these cation vacancy clusters have a similar segregation behavior as V_{Ce}, where the segregation energies are more negative in Ce_{-1} and Ce_0 layers. These results suggest that, under equilibrium conditions, the existence of GBs makes it easier for fission products to be trapped, such as Xe, in the GB region compared with that in the bulk. In addition, our calculations show that the influence of the charge states of these trap sites on their segregation behavior is negligible.

3.3 Segregation and solution profile of Xe

The segregation behavior of Xe is studied by placing one Xe atom at one of the above trap sites at the GB. Since the most stable charge state for the trap sites, within a wide range of Fermi levels, is the formal charge state, we will mainly focus on these trap sites for Xe substitution, such as Xe_{Ce}^{4-}, $(Xe_{Ce}\text{-}V_O)^{2-}$, $(Xe_{Ce}\text{-}2V_O)^0$, as shown in Fig. 4. The results show that Xe is more energetically favorable to substitute at the trap sites and segregate to Ce_0 and Ce_{-1} layers, suggesting that Xe prefers to reside at the GB in certain layers, which is consistent with previous theoretical results in UO_2 [26]. These results are understandable since the sites in these Ce layers are adjacent to the large free volume due to the removal of one O layer in constructing the boundary, which can provide more space for segregation than in the bulk, as discussed in section 3.1. This uniquely structural effect is reversed as more vacancies segregate around the Xe atoms. For example, in Ce_{-1} layer, $E_{seg}((Xe_{Ce})^{4-})$ is -2.43 eV, $E_{seg}((Xe_{Ce}\text{-}V_O)^0)$ decreases to -1.37 eV, and $E_{seg}((Xe_{Ce}\text{-}2V_O)^0)$ is only -0.72 eV. To avoid the finite-size effect on these results, we have also considered defects in larger supercells, with 432 and 480 atoms, and obtained a similar trend, as shown in Fig. S6. These results indicate that, as the size of trap sites increases, the formation energy of a Xe atom trapped in these sites at GBs would become comparable to that in the bulk, and thus the segregation capacity of Xe near the GBs is decreased.

Since the segregation energy is the driving force for Xe atoms to migrate from the bulk to more stable sites at GBs, the small segregation energy of Xe at these large-size trap sites may restrict the aggregation of Xe into the GB region, especially in polycrystalline fuels. However, in nanostructured fuels, due to the small grain size, irradiation damage is more likely to occur near the GBs [8], and thus fission products may directly occupy the sites

at GBs, leading to bubble formation. Besides the segregation profile of fission products near the GBs, we have studied further the solution profile in order to understand the stability and solubility of fission products trapped near the GB at different stoichiometric conditions.

The solution energy of one Xe atom in a trap site with a formal charge state is calculated as a function of oxygen chemical potential, as shown in Fig. 5. For comparison, the solution energies for Xe trapped in the bulk are also determined. Here, we only show the lowest solution energies for these defects. For example, the lowest solution energy for Schottky defects in the bulk is the $(V_{Ce}\text{-}2V_O)^0$ with V_Os along [100] direction, as shown in Table SI, which is consistent with previous results [25]. It is observed that the solution energies, both in the bulk and GB, change dramatically in different stoichiometric conditions, which is consistent with previous calculations in UO_2 [21, 23]. Under hypo-stoichiometric (Ce-rich) conditions, the most favorable site for Xe trapping is the Schottky defect $(V_{Ce}\text{-}2V_O)^0$; and under hyper-stoichiometric (O-rich) conditions, it is the V_{Ce}^{4-}. In addition, the solubility of Xe near the GB is higher than that in the bulk, especially under hyper-stoichiometric conditions, which is associated with the strong segregation property of Xe_{Ce} at the GB, as discussed above. Considering the significant segregation behavior of Xe and the corresponding trap sites near the GB, we can reasonably assume that under hyper-stoichiometric conditions the Xe concentration should be higher at GBs than in the bulk, which may enhance the formation of gas bubbles near the GB. In the following, we will study Xe diffusion both in the bulk and at the GB to further confirm our assumption.

3.4 Diffusion behavior of Xe

Previous theoretical investigations of fission gas in UO_2 have confirmed that when one Xe atom occupies a trap site (Xe_V, here we use V to denote the possible vacancy trap sites depending on the stoichiometry), it diffuses only by binding a second cation vacancy to form a Xe_V/V_U cluster [12, 14, 21, 23, 46], and Xe diffusion in the samples is mainly determined by the diffusion of the Xe_V/V_U cluster [21, 23, 46]. In addition, based on DFT calculations, Andersson et al. have reported that the rate limiting step for the diffusion of Xe_V/V_U cluster is the migration of the second V_U within the cluster, in which Xe spontaneously diffuses with the motion of the second V_U [21, 46]. In CeO_2, however, when considering the different resistance against of oxidation of UO_2 and CeO_2 [20, 25], the diffusion behavior of cation vacancy and Xe atom may be different. In order to identify the diffusion behavior of Xe in CeO_2, the following studies are carried out.

Based on previous studies [21, 23, 46], when a second cation vacancy is attracted by the Xe_V, it either detaches from the cluster or jumps to a new position within the cluster. In the first case, our calculation results show that the binding energies of the Xe_V/V_{Ce} cluster in CeO_2 are around -1.32 eV, indicating that the bound cation vacancy around the Xe_V is more stable and difficult to diffuse away from the cluster, which is consistent with that in UO_2 [21]. In the latter case, due to the strong resistance against oxidation in CeO_2 [25], the behavior of Xe atom in CeO_2 is slightly different from that in UO_2 [21], where the Xe atom doesn't diffuse with the motion of the second V_{Ce} within the cluster, as shown in Fig. 6. However, our calculations show that the diffusion barriers for the Xe atom within the cluster are at least 1 eV lower than those for the diffusion of cation vacancies both in the bulk and near GBs, indicating that the rate limiting step for Xe diffusion in CeO_2 is still related to the migration of the second cation vacancy within the cluster, which is

identical to that in UO_2 [21, 23, 46]. These results suggest that, although the significant difference in oxidation resistance in CeO_2 and UO_2 may differentiate the behavior of Xe atom within the cluster, the diffusion mechanism of Xe in both compounds are comparable to each other.

Moreover, the migration barriers for the V_{Ce} within the Xe_V/V_{Ce} cluster in the bulk and at the GB are calculated and summarized in Table II. It is observed that the migration barriers along the Σ3 GB are smaller than those in the bulk, indicating that the mobility of the Xe_V/V_{Ce} cluster near the Σ3 GB is higher than that in the bulk. When considering the generally significant segregation of cation vacancies and Xe near the Σ3 GB, the results confirm that the diffusive of Xe along the Σ3 GB should be higher than that in the bulk, which further enhances the accumulation of Xe atoms near the Σ3 GB. Furthermore, given that the Σ3 GB provides an approximate lower bound on defect diffusion [32, 33], it is reasonable to assume that other higher-energy GBs are more likely to enhance the Xe diffusion and bubble formation. This is consistent with previously experimental results in CeO_2 [9], which found that the density of krypton (Kr) bubbles near the GBs are larger than that in the interior grain region. Since the properties of Kr and Xe are similar to each other, the density of Xe bubbles near the GB could be also higher than that in the interior grain region.

4. Conclusion

In this study, we investigated the segregation properties of cation vacancies and vacancy clusters, i.e., di-vacancy and Schottky defects, as well as the behavior of the fission gas,

Xe, near the CeO_2 grain boundary. Significant segregation behavior for the V_{Ce} is observed near the GB, regardless of the charge states. Specifically, segregation energies in the Ce_{-1} layer are -0.84 eV to -1.66 eV, followed by the energies in the Ce_0 layer of about -0.79 to -1.29 eV. These results are associated with the local atomic structure near the GB, resulting in weaker bond strength and more negative segregation energies in these layers. For the V_{Ce} in other layers, the energies are close to zero, approaching bulk behavior. Similar segregation profiles can also be found for the vacancy clusters. These findings suggest that the existence of GBs provides more potential trap sites for fission gases, such as Xe, than in the bulk under equilibrium conditions.

For segregation of Xe atoms, our results show that Xe is more energetically favorable to substitute at the trap sites and segregate near the GB, which is attributed to the larger free volume available in the GB as compared to the bulk. As the size of trap sites increases, the segregation capacity of Xe is reduced, i.e., the formation energies of a Xe atom trapped in these sites would be comparable in the bulk and GB.

For Xe diffusion behavior in irradiated-ceria, the work is focused on the V_{Ce}-assisted mechanism and compared with that in UO_2. We found that the diffusion mechanism of Xe in CeO_2 is comparable to that in UO_2. Our calculations show that the diffusion activation energies in the Σ3 GB are lower than those in the bulk, suggesting that the diffusivity of Xe atom is higher at the GB than that in the bulk, which further enhances the aggregation of Xe atoms near the GB.

Acknowledgments

This research was supported by the DOE Office of Nuclear Energy's Nuclear Energy University Programs (NEUP). The theoretical calculations were performed using the supercomputer resources at the National Energy Research Scientific Computing Center, supported by the Office of Science, US Department of Energy under Contract No. DEAC02-05CH11231.

[1] W. J. Weber, A. Navrotsky, S. Stefanovsky, E. R. Vance, and E. Vernaz, MRS Bull., 34 (2009) 46-53.

[2] G. Ackland, Science 327 (2010) 1587-1588.

[3] J. Spino, H. Santa Cruz, R. Jovani-Abril, R. Britcher, C. Ferrero, J. Nucl. Mater. 422 (2012) 27-44.

[4] T. E. Chung, T. J. Davies, J. Nucl. Mater. 79 (1979) 143.

[5] J. Spino, H. Santa Cruz, R. Birtcher, C. Ferrero, R. Pierritz, A. Fernandez, Workshop on Radiation Stability of Complex Microstructures, Santa Fe, USA, September 02-04, 2008.

[6] Y. Zhang, W. Jiang, C. Wang, F. Namavar, P. D. Edmondson, Z. Zhu, F. Gao, J. Lian, and W. J. Weber, Phys. Rev. B 82 (2010) 184105.

[7] Y. Zhang, P. D. Edmondson, T. Varga, S. Moll, F. Namavar, C. Lan, and W. J. Weber, Phys. Chem. Chem. Phys., 13 (2011) 11946-11950.

[8] S. Dey, J. W. Drazin, Y. Wang, J. A. Valdez, T. G. Holesinger, B. P. Uberuaga, and R. H. Castro, Sci. Rep. 5 (2015) 7746.

[9] L. He, C. Yablinsky, M. Gupta, J. Gan, M. A. Kirk, and T. R. Allen, Nuclear Technology 182 (2013) 164-169.

[10] J. Xi, B. Liu, Y. Zhang, W. J. Weber, Comput. Mater. Sci., 123 (2016) 131-138.

[11] C. R. A. Catlow, Radiat. Eff. Defects Solids 53 (1980) 127.

[12] R. G. J. Ball and R. W. Grimes, Chem. Soc. Faraday Trans. 86 (1990) 1257.

[13] R. W. Grimes and C. R. A. Catlow, Philos. Trans. R. Soc. London Ser. A 335 (1991) 609.

[14] R. G. J. Ball and R. W. Grimes, J. Nucl. Mater. 188 (1992) 216-221.

[15] K. Govers, S. Lemehov, M. Verwerft, J. Nucl. Mater. 405 (2010) 252-260.

[16] S. T. Murphy, A. Chartier, L. VanBrutzel, J.-P. Crocombette, Phys. Rev. B 85 (2012) 144102.

[17] S. Nicoll, H. Matzke, C. R. A. Catlow, J. Nucl. Mater. 226 (1995) 51-57.

[18] A. E. Thompson, C. Wolverton, Phys. Rev. B 87 (2013) 104105.

[19] Y. Yun, H. Kim, H. Kim, K. Park, J. Nucl. Mater. 378 (2008) 40-44.

[20] Y. Yun, P. M. Oppeneer, H. Kim, K. Park, Acta Mater. 57 (2009) 1655-1659.

[21] D. A. Andersson, B. P. Uberuaga, P. V. Nerikar, C. Unal, C. R. Stanek, Phys. Rev. B 84 (2011) 054105.

[22] X. Y. Liu, B. P. Uberuaga, D. A. Andersson, C. R. Stanek, K. E. Sickafus, Appl. Phys. Lett. 98 (2011) 151902.

[23] E. Vathonne, D. A. Andersson, M. Freyss, R. Perriot, M. W. D. Cooper, C. R. Stanek, and M. Bertolus, Inorg. Chem. 56 (2017) 125-137.

[24] M. Freyss, N. Vergnet, T. Petit, J. Nucl. Mater. 352 (2006) 144-150.

[25] H. Y. Xiao, Y. Zhang, W. J. Weber, J. Nucl. Mater. 414 (2011) 464-470.

[26] P. V. Nerikar, D. C. Parfitt, L. A. Casillas Trujillo, D. A. Andersson, C. Unal, S. B. Sinnott, R. W. Grimes, B. P. Uberuaga, and C. R. Stanek, Phys. Rev. B 84 (2011) 174105.

[27] W. J. Weber, Radiat. Eff., 83 (1984) 145.

[28] H. Kleykamp, J. Nucl. Mater. 307-311 (2002) 749.

[29] K. Yasunaga, K. Yasuda, S. Matsumura, T. Sonoda, J. Nucl. Mater. 250 (2006) 114.

[30] B. Ye, M. A. Kirk, W. Chen, A. Oaks, J. Rest, A. Yacout, J. F. Stubbins, J. Nucl. Mater. 414 (2011) 251-256.

[31] P. Lejcek and S. Hofmann, Crit. Rev. Solid State 20 (1995) 1.

[32] M. Mendelev, H. Zhang, and D. Srolovitz, J. Mater. Res. 20 (2005) 1146.

[33] C. Minkwitz, C. Herzig, E. Rabkin, and W. Gust, Acta. Mater. 47 (1999) 1231.

[34] G. Kresse and D. Joubert, Phys. Rev. B 59 (1999) 1758.

[35] J. P. Perdew and A. Zunger, Phys. Rev. B 23 (1981) 5048.

[36] A. I. Liechtenstein, V. I. Anisimov, and J. Zaanen, Phys. Rev. B 52 (1995) R5467.

[37] C. W. M. Castleton, J. Kullgren, and K. Hermansson, J. Chem. Phys. 127 (2007) 244704.

[38] M. Wolcyrz, L. Kepinski, J. Solid State Chem. 99 (1992) 409.

[39] B. Feng, H. Hojo, T. Mizoguchi, H. Ohta, S. D. Findlay, Y. Sato, N. Shibata, T. Yamamoto, and Y. Ihuhara, Appl. Phys. Lett. 100 (2012) 073109.

[40] F. Yuan, B. Liu, Y. Zhang, W. J. Weber, J. Phys. Chem. C, 120 (2016) 6625.

[41] G. Henkelman, B. P. Uberuaga, and H. Jonsson, J. Chem. Phys., 113 (2000) 9901.

[42] J. Xi, H. Xu, Y. Zhang, W. J. Weber, Phys. Chem. Chem. Phys. 19 (2017) 6264-6273.

[43] J. Xi, B. Liu, F. Lin, Y. Zhang, W. J. Weber, Scr. Mater 139 (2017) 1-4.

[44] B. Liu, V. R. Cooper, Y. Zhang, W. J. Weber, Acta. Mater. 90 (2015) 394-399.

[45] H. F. Wang, X. Q. Gong, Y. L. Guo, Y. Guo, G. Z. Lu, and P. Hu, J. Phys. Chem. C. 113 (2009) 10229-10232.

[46] D. A. Andersson, P. Garcia, X. Y. Liu, G. Pastore, M. Tonks, P. Millett, B. Dorado, D. R. Gaston, D. Andrs, R. L. Williamson, R. C. Martineau, B. P. Uberuaga, C. R. Stanek, J. Nucl. Mater. 451 (2014) 225-242.

Table I. The chemical potential for oxygen and cerium in CeO_2 calculated using LDA+*U* under different stoichiometry conditions.

Stoichiometry	μ_{Ce} (eV)	μ_{O} (eV)
O-poor/Ce-rich	-6.89	-9.83
O-rich/Ce-poor	-18.05	-4.25
Stoichiometric	-12.47	-7.04

Table II. The migration barrier, E_m2, (eV) of V_{Ce} within the Xe_V/V_{Ce} cluster. The values in the parentheses are the barriers in the opposite direction.

	$E_m2(Xe_{VCe}/V_{Ce})$	$E_m2(Xe_{VCe\text{-}2VO}/V_{Ce})$
Σ3 GB	3.08(3.08)	2.17(2.48)
Bulk	4.23(4.23)	4.26(5.09)

Fig. 1. The configuration of the $\Sigma 3(111)/[1\bar{1}0]$ tilt GB (O: grey, Ce: red). The green line represents the cation mirror plane, and the blue line is the anion mirror plane. Numbers indicate the cation layer number for the possible cation vacancy position.

Fig. 2. (a) Segregation energies of V_{Ce} with different charge states, (b) the bond (E_{bond}) and relaxation (E_{relax}) energies of V_{Ce}^{0} in the $\Sigma 3$ (111)/ $[1\bar{1}0]$ tilt GB as a function of the cation layer as defined in Fig. 1.

Fig. 3. (a) Segregation profile of cation vacancy and vacancy clusters with formal charge states; (b) and (c) the lowest segregation energy of $(V_{Ce}\text{-}V_O)^q$ and $(V_{Ce}\text{-}2V_O)^0$, respectively, as a function of the cation layer near the $\Sigma 3$ (111)/ $[1\bar{1}0]$ tilt GB as defined in Fig. 1.

Fig. 4. Segregation profile of Xe at above trap sites as a function of the cation layer near the $\Sigma 3$ (111)/ $[1\bar{1}0]$ tilt GB as defined in Fig. 1.

Fig. 5. Solution energies of Xe at above trap sites at formal charge states in the bulk and at GB. Fermi level is taken to be 1.32 eV at the middle of the band gap.

Fig. 6. Schematic picture of the diffusion mechanism associated with moving the Xe_V/V_{Ce} cluster within (111) plane. The oxygen sublattices are omitted for clarification. Arrows indicate directions where atoms will move to form the next configurations.

Fig.1

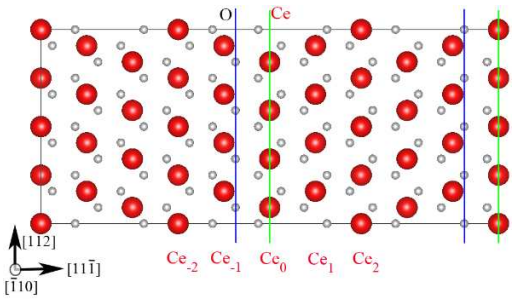

Fig. 2

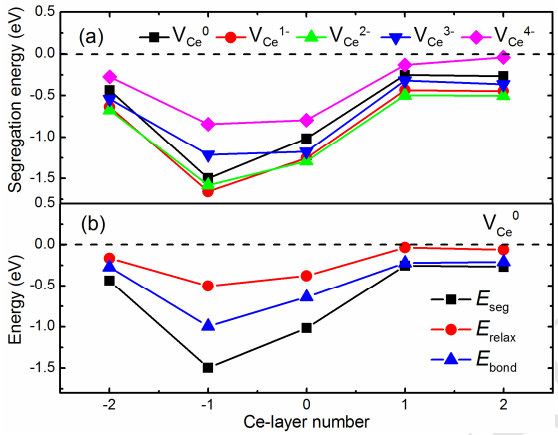

Fig. 3

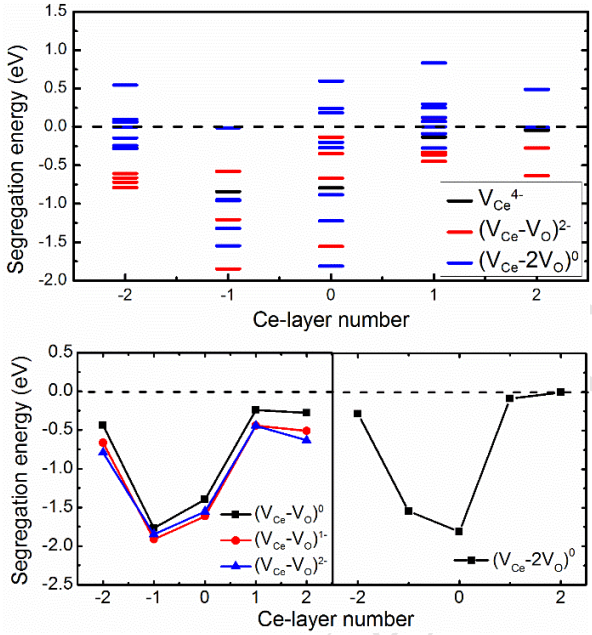

Fig. 4

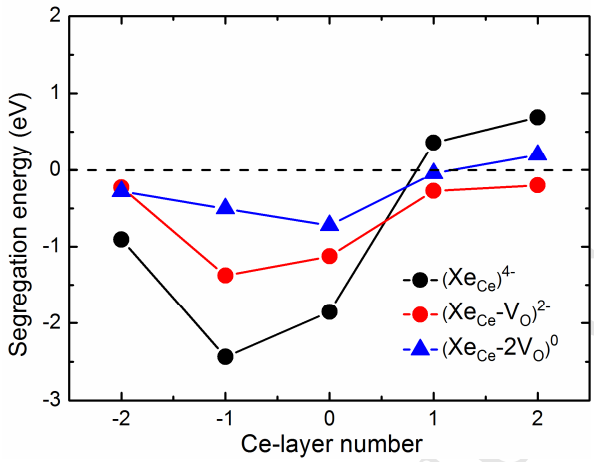

Fig. 5

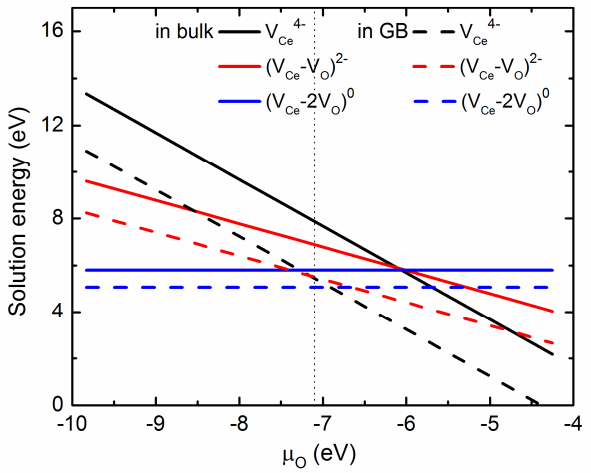

Fig. 6

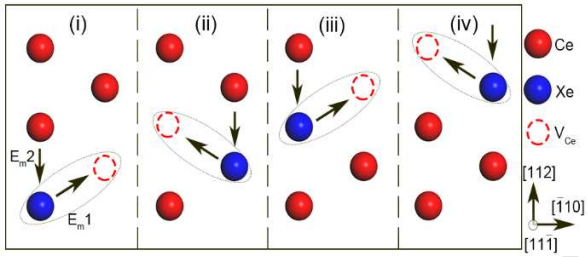

- Segregation profile of Xe and trap sites near grain boundary in CeO_2 are studied
- The segregation propensity of Xe is reduced as the size of trap sites increases
- The diffusion mechanism of Xe in CeO_2 is comparable to that in UO_2
- The existence of grain boundaries in CeO_2 enhances the aggregation of Xe atoms